https://doi.org/10.5194/tc-2019-129
Preprint. Discussion started: 25 June 2019

The Cryosphere Discussions
Open Access
EGU

West Greenland ice sheet retreat history reveals elevated precipitation during the Holocene thermal maximum

Jacob Downs[1], Jesse Johnson[2], Jason Briner[3], Nicolás Young[4], Alia Lesnek[3], and Josh Cuzzone[5]

[1]Department of Mathematical Sciences, University of Montana, Missoula MT, USA
[2]Department of Computer Science, University of Montana, Missoula MT, USA
[3]Department of Geology, University at Buffalo, Buffalo NY, USA
[4]Lamont-Doherty Earth Observatory, Columbia University, Palisades NY, USA
[5]Department of Earth System Science, University of California Irvine, Irvine CA, USA

Correspondence: Jacob Downs (jacob.downs@umontana.edu)

Abstract. We investigate changing precipitation patterns in the Kangerlussuaq region of west central Greenland during the Holocene thermal maximum, using a new chronology of ice sheet terminus position through the Holocene and a novel inverse modeling approach based on the unscented transform (UT). The UT is applied to estimate changes in annual precipitation in order to reduce the misfit between modeled and observed terminus positions. We demonstrate the effectiveness of the UT for time-dependent data assimilation, highlighting its low computational cost and trivial parallel implementation. Our results indicate that Holocene warming coincided with elevated precipitation, without which modeled retreat in the Kangerlussuaq region is more rapid than suggested by observations. Less conclusive is if high temperatures during the HTM were specifically associated with a transient increase in precipitation, as the results depend on the assumed temperature history. The importance of precipitation in controlling ice sheet extent during the Holocene underscores the importance of Arctic sea ice loss and changing precipitation patterns ~~on~~ the future stability of the GrIS.

1 Introduction

During the early Holocene (∼11.7 - 8 ka BP), terrestrial and marine climate proxies from the northern hemisphere reveal a warmer than present peak in temperature (Kaufman et al., 2004; Marcott et al., 2013). This period of elevated temperatures, likely initiated by greater than modern insolation, is referred to as the Holocene thermal maximum (HTM). Its onset, duration, and severity likely depend on ~~location~~ (Kaufman et al., 2004). Records of HTM warming can be found in Greenland ice core ~~records~~. For example, temperatures measured in the Dye-3 borehole show a pronounced HTM signal occurring from 7 to 4 ka BP and having value of 2.5° above present temperatures (Dahl-Jensen et al., 1998; Miller et al., 2010), whereas at the GISP2 site, the HTM appears to occur slightly earlier, following the 8.2 ka BP cold event (Kobashi et al., 2017) (Figure 1). Recently, Buizert et al. (2018) merged climate ~~model~~ model output and ice core records to create a spatially explicit reconstruction of Holocene temperature for all of Greenland.

While warming during the HTM is well established, less is known about the patterns of ~~precipitation~~ that accompanied increased temperatures. Ice core records provide long term estimates of accumulation (Alley et al., 1993), but these point

https://doi.org/10.5194/tc-2019-129
Preprint. Discussion started: 25 June 2019

measurements near ice divides are not representative of the precipitation across the ice sheet, particularly at lower elevations near the coast. Because the HTM was accompanied by lower Arctic sea ice extent (Polyak et al., 2010), it is possible that additional moisture was available to the GrIS from open Arctic waters. This is supported by proxy evidence showing an increase in winter precipitation in western Greenland coincident with HTM warming (Thomas et al., 2016). However, ~~temperature is known with greater certainty than precipitation.~~

Understanding feedbacks between temperature and precipitation during the HTM has implications for the future of the GrIS. ~~Warming~~ and declining sea ice are projected to cause an increase in Arctic precipitation (Bintanja and Selten, 2014; Singarayer et al., 2006). In the near future, climatic conditions in Greenland may be similar those that are believed to have occurred during the HTM. The history of retreat in west central Greenland therefore provides a means of assessing the stability of a warmer and possibly wetter future GrIS.

Previous modeling studies indicate that retreat in land terminating regions of the GrIS were controlled primarily by surface mass balance rather than ice dynamics (Cuzzone et al., 2019; Lecavalier et al., 2014). Enhanced precipitation may have stabilized the ice sheet during the HTM by increasing overall surface mass balance due to elevated winter snowfall (Thomas et al., 2016), or accelerated retreat due to the presence of more surface water in summer.

In this work, we investigate changes in precipitation patterns in the Kangerlussuaq region of the west central GrIS during the HTM, taking advantage of a new chronology of ice sheet terminus position through the Holocene (Young et al., 2019, In Review) and a novel inverse modeling approach based on the unscented transform (UT) (Julier and Uhlmann, 1997). In particular, we use the UT to estimate changes in annual precipitation during the Holocene by reducing the misfit between modeled and observed terminus positions in a flowline ice dynamics model (Brinkerhoff et al., 2017) (Section 2.1).

The inverse problem is posed as a Bayesian inference problem, and its solution involves estimating the mean and covariance of a non-Gaussian posterior probability distribution. The unscented transform provides a computationally efficient and trivially parallelizable alternative to Markov Chain Monte Carlo methods such as Metropolis Hastings method (Chib and Greenberg, 1995) for estimating the statistics of the posterior distribution. Even state-of-the-art MCMC methods require drawing many thousands of random samples, each of which corresponds to a single forward run of the ice dynamics model. In contrast, the UT uses a small, fixed number of deterministic sample points for estimate the mean and covariance of the posterior distribution (Section 2.5.1). .

2 Numerical methods for inference

2.1 Ice-sheet model

We use the 1D, isothermal, flowline model with higher-order momentum balance described in Brinkerhoff et al. (2017). The momentum conservation equations are simplified using the Blatter-Pattyn approximation, assuming hydrostatic pressure and negligible vertical resistive stresses (Blatter, 1995; Pattyn, 2003). Default parameter values used in this work are specified in Table 1.

https://doi.org/10.5194/tc-2019-129
Preprint. Discussion started: 25 June 2019


The Cryosphere Discussions

We adopt a linear sliding law of the form

$$\tau_b = \beta^2 N u_b \tag{1}$$

where τ_b is basal shear stress, β^2 is basal traction, N is effective pressure, and u_b is sliding speed. Basal water pressure is assumed to be a fixed fraction $P_{frac} = 0.85$ of the ice overburden pressure. Effective pressure is given by

$$N = P_0 - P_w = P_0 - P_{frac} P_0 \tag{2}$$

where P_0 is the ice overburden pressure and P_w is basal water pressure. Basal traction is tuned so that surface velocities roughly match observations from Mouginot et al. (2017) for modern Isunnguata Sermia.

2.2 Positive degree day model

Surface mass balance is estimated using a positive degree day (PDD) model (Johannesson et al., 1995). Inputs into the PDD model include the unknown ice surface elevation S, modern monthly temperature T_m and precipitation P_m along the flowline, as well as the temperature anomaly ΔT. Modern temperature and precipitation are computed as 30 year averages from 1980-2010 using Box (2013). Monthly temperature anomalies, computed as averages along the flowlines, are computed at 20 year intervals using the Buizert et al. (2018) temperature reconstruction.

Surface temperature T is computed monthly as

$$T = T_m + \Delta T + \alpha(S - S_m) \tag{3}$$

where S_m is the modern surface elevation, and $\alpha = 5$ °C km^{-1} is the lapse rate. Following Ritz et al. (2001), precipitation P along the flowline is given by

$$P = P_m \exp\left(\lambda_p (T - T_m)\right) + \Delta P. \tag{4}$$

We take $\lambda_p = 0.07$, which corresponds to a doubling of precipitation for every 1 °C increase in temperature above modern. Here, we also introduce a precipitation anomaly function ΔP, analagous to the temperature anomaly function ΔT. This time-dependent function is used to adjust precipitation in order to reduce mismatch between modeled and observed terminus positions. Unlike ΔT, which is known from extensions of ice core data (Buizert et al., 2018), ΔP will be used as a control variable to be determined using the inverse methods detailed in Section 2.5.2. Equations 3 and 4 provide a method of accounting for elevation changes through time and downscaling inputs to match the mesh resolution of the model ($\sim$ 1 km).

Positive degree days and snowfall are computed month-by-month based on mean monthly temperature and precipitation (Johannesson et al., 1995). Snow is melted first at a rate of 5×10^{-3} meters water equivalent (m.w.e.) per degree day followed by ice at a rate of 8×10^{-3} m.w.e. per degree day. Snow melt is initially supposed to refreeze in the snowpack as superimposed ice. Runoff begins when the superimposed ice reaches a given fraction (60%) of the snow cover (Reeh, 1991).

https://doi.org/10.5194/tc-2019-129
Preprint. Discussion started: 25 June 2019

2.3 Flowline Selection and Moraine Age Constraints

To define the path followed by ice, we assume ice flow follows the modern surface velocity field inland of the present day margin. In ice free regions, the direction of ice flow is inferred from bedrock topography (Figure 1). Since the direction of ice flow is unknown and time varying, we cannot directly quantify the uncertainty introduced by errors in flowline selection. To account for some of this uncertainty, we perform inversions on two plausible, adjacent paleo-flowlines in the Kangerlussuaq area.

The rate of Holocene retreat on each flowline is estimated using constraints on ice sheet terminus position from (Young et al., 2019, In Review) (Figure 1). Terminus position data in Young et al. (2019, In Review) indicates that in the early Holocene (11.6 ka BP), the ice sheet margin was some tens of kilometers inland of the present day coastline. Although the moraine patterns are spatially complex, generally speaking, there was a period of moderate retreat ($\sim$10 km on the northern flowline and $\sim$30 km on the southern flowline) from 11.6 to 10.3 ka BP, followed by rapid retreat ($\sim$100 km on both flowlines) from 10.3 to 8.1 ka BP. By 8.1 ka BP, the margin position was within 20 km of its present position on both paleo-flowlines (Figure 3). The ~~the~~ modern terminus position provides one additional constraint.

2.4 Modeling Approach

Model runs are initialized by tuning the precipitation anomaly to obtain a steady state margin position 5 km beyond the 11.6 ka BP moraine using a fixed temperature anomaly corresponding to 12.6 ka BP. We then invert for a precipitation anomaly time series that forces a steady rate of retreat of 5 km over 1000 years, using the methods in Section 2.5.2, to obtain an initial ice sheet configuration with the correct terminus position at 11.6 ka BP. This initialization procedure is intended to ease the ice sheet out of steady state in order to avoid strong transient effects at the beginning of model runs.

Reconstructions of relative sea level from Caron et al. (2018), along with the retreat chronology in Young et al. (2019, In Review), indicate that ice remained grounded on both the northern and southern flowlines from 11.6 ka BP onward (Figure 2). Evidence suggests the terminus was terrestrial during this period in spite of changes in sea level and bedrock elevation due to isostatic uplift. As such, isostatic effects are neglected in the model.

2.5 Data Assimilation Approach

In order to assess the initial mismatch between modeled and observed terminus positions, we perform a reference experiment using temperature anomalies from Buizert et al. (2018) and a precipitation anomaly $\Delta P = 0$ (Section 3.1). To improve the fit from this initial run, we assimilate terminus position observations to obtain improved estimates of the Holocene precipitation anomaly.

Previous modeling studies indicate that retreat in land-terminating sectors of the GrIS were dominated by surface mass balance rather than ice dynamics (Cuzzone et al., 2019; Lecavalier et al., 2014). Thus, uncertainty in Holocene climate and thus surface mass balance is likely the primary cause of discrepancies between modeled and observed terminus positions.

https://doi.org/10.5194/tc-2019-129
Preprint. Discussion started: 25 June 2019

The Cryosphere Discussions
Open Access
EGU

Table 1. Summary of primary model parameters used in this work. Default values are provided where applicable. Prior parameter uncertainties assumed for the sensitivity test are shown in the 2σ column.

Description	Symbol	Value	2σ Range	Units
PDD Model Parameters				
Std. deviation	σ	5.5	-	C
Std. deviation, accumulation	σ_a	5	-	C
Ablation rate, snow	λ_s	5×10^{-3}	3 - 7 $\times10^{-3}$	m.w.e. C^{-1} d^{-1}
Ablation rate, ice	λ_i	8×10^{-3}	6 - 10 $\times10^{-3}$	m.w.e. C^{-1} d^{-1}
Precipitation param.	λ_p	7 $\times10^{-2}$	3 - 11 $\times10^{-2}$	C^{-1}
Superimposed ice fraction	p_{max}	0.6	-	-
Ice Flow Parameters				
Rate factor	A	3.5 $\times10^{-25}$	2.8 - 4.2 $\times10^{-25}$	s^{-1} Pa^{-3}
Basal traction	β^2	1.6×10^{-3}	1.44 - 1.76 $\times10^{-3}$	Pa a m^{-1}
Water pressure fraction	P_{frac}	0.85	-	-
Unscented Transform Parameters				
State vector dimension	n	45	-	-
Prior smoothness param.	δ	5 $\times$ 10^3	-	-
Sigma Scaling param.	w_0	0.5	-	-

Table 2. Citations for the primary data sets used in this work.

Data	Citation
Terminus position chronology	Young et al. (2019, In Review)
Bedrock elevation	Morlighem et al. (2017)
Modern ice surface velocity	Mouginot et al. (2017)
Modern precipitation	Box (2013)
Temperature reconstructions	Buizert et al. (2018)
	Dahl-Jensen et al. (1998)
Relative sea level	Caron et al. (2018)

https://doi.org/10.5194/tc-2019-129
Preprint. Discussion started: 25 June 2019


The Cryosphere Discussions
Open Access
EGU

In principle, both temperature and precipitation anomalies could be tuned to improve the fit between modeled and observed terminus positions. However precipitation is a natural choice since it is more poorly constrained than temperature.

In the upcoming sections, we outline our approach for estimating precipitation anomalies given measured terminus positions. We introduce a framework for time-dependent data assimilation based on the unscented transform (UT) (Julier and Uhlmann, 1997). Section 2.5.1 outlines the basic tenets of the unscented transform. Sections 2.5.2 - 2.5.6 outline how the unscented transform can be applied directly to the problem of time-dependent data assimilation.

2.5.1 Overview of the Unscented Transform

Suppose that $\boldsymbol{x}$ is an n-dimensional Gaussian random variable with mean vector $\bar{\boldsymbol{x}}$ and covariance matrix P_x, and $\mathcal{F} : \mathbb{R}^n \rightarrow \mathbb{R}^m$ is a nonlinear function. We would like to compute the mean $\bar{\boldsymbol{y}}$ and covariance matrix P_y of the transformed random variable

$$\boldsymbol{y} = \mathcal{F}(\boldsymbol{x}). \tag{5}$$

In general, the mean and covariance of the non-Gaussian probability distribution $P(\boldsymbol{y})$ can be approximated using Markov chain Monte Carlo (MCMC) methods such as the Metropolis-Hastings algorithm (Chib and Greenberg, 1995). As a computationally efficient alternative to MCMC methods, Julier and Uhlmann (1997) introduced a method for approximating the mean and covariance of $P(\boldsymbol{y})$ called the unscented transform (UT).

A set of vectors, called sigma points, are chosen with the same weighted sample mean and weighted covariance structure as $\boldsymbol{x}$. There are many algorithms for generating sigma points sets with different numbers of points. A commonly used set of $2n+1$ sigma points is given by

$$\boldsymbol{\chi_i} = \begin{cases} \boldsymbol{x_0} & i = 0 \\ \boldsymbol{x_0} - \sqrt{n+\kappa}[\sqrt{P_x}]_i & i = 1, \cdots, n \\ \boldsymbol{x_0} + \sqrt{n+\kappa}[\sqrt{P_x}]_i & i = n+1, \cdots, 2n \end{cases} \tag{6}$$

with corresponding weights given by

$$w_i = \begin{cases} \kappa/(n+\kappa) & i = 0 \\ 1/2(n+\kappa) & \text{otherwise} \end{cases}. \tag{7}$$

The notation $\left[\sqrt{P_x}\right]_i$ refers to the i-th row of a matrix square root (typically computed by Cholesky factorization) of P_x, and κ is a free parameter controlling the scaling of the sigma points around the mean. Julier and Uhlmann (1997) recommend a default value of $\kappa = 3 - n$. However, κ can be fine tuned to reduce prediction errors for a given problem.

The nonlinear function $\mathcal{F}$ is applied to each sigma point to yield a set of transformed points

$$\boldsymbol{\mathcal{Y}_i} = \mathcal{F}(\boldsymbol{\chi_i}). \tag{8}$$

The mean and covariance of $P(\boldsymbol{y})$ are then estimated as weighted sums

$$\bar{\boldsymbol{y}} = \sum_{i=0}^{2n} w_i \boldsymbol{\mathcal{Y}_i} \tag{9}$$

https://doi.org/10.5194/tc-2019-129
Preprint. Discussion started: 25 June 2019

$$P_y = \sum_{i=0}^{2n} w_i (\boldsymbol{\mathcal{Y}_i} - \bar{\boldsymbol{y}})(\boldsymbol{\mathcal{Y}_i} - \bar{\boldsymbol{y}})^T. \tag{10}$$

The unscented transform ~~is known~~ primarily in the context of the unscented Kalman filter. However, the UT can be applied more generally as an alternative to traditional MCMC methods. Sigma points and weights sets are designed to estimate the first two statistical moments (mean and covariance) of the non-Gaussian distribution $P(\boldsymbol{y})$ using a minimal number of function evaluations.

2.5.2 Data Assimilation using the Unscented Transform

Here, we outline how the unscented transform is applied to estimate precipitation anomalies. Time-dependent data assimilation using the UT involves running the ice sheet model with a set of different precipitation anomaly histories, each corresponding to a different sigma point. This is followed by a post-processing step, which incorporates the ice sheet terminus chronology data via a Kalman filter type correction of the prior mean vector and covariance matrix. Implementation of the unscented transform is straightforward and easily parallelizable since each model run is independent.

In what follows, the notation $\boldsymbol{x} \sim \mathcal{N}(\boldsymbol{x_0}, P_x)$ means that the random variable $\boldsymbol{x}$ is Gaussian or normally distributed with mean $\boldsymbol{x_0}$ and covariance P_x. Let $\boldsymbol{\Delta p}$ be an n-dimensional discretization of the unknown precipitation anomaly history ΔP at regular time intervals, $\boldsymbol{\ell}$ be an m-dimensional vector of glacier length observations through time, and $\mathcal{F} : \mathbb{R}^n \to \mathbb{R}^m$ be a nonlinear function that maps temperature and precipitation forcings to glacier length measurements via the ice dynamics and PDD models. Given a multivariate Gaussian prior $\boldsymbol{\Delta p} \sim \mathcal{N}(\boldsymbol{\Delta p_0}, P_0)$ with mean $\boldsymbol{\Delta p_0}$ and covariance matrix P_0, we would like to estimate the mean and covariance of the posterior distribution

$$P(\boldsymbol{\Delta p}|\boldsymbol{\ell}) \propto P(\boldsymbol{\ell}|\boldsymbol{\Delta p})P(\boldsymbol{\Delta p}). \tag{11}$$

Suppose that

$$\boldsymbol{\ell} = \mathcal{F}(\boldsymbol{\Delta p}) + \mathbf{r} \tag{12}$$

where $\mathbf{r} \sim \mathcal{N}(\mathbf{0}, R)$ represents the measurement noise. The unscented transform is applied to estimate the joint distribution of $[\boldsymbol{\Delta p}\, \boldsymbol{\ell}]^T$ as a multivariate Gaussian distribution. To reduce computational costs, we use a minimal set of $n+1$ sigma points $\boldsymbol{\mathcal{P}_i}$ with corresponding weights w_i generated using the method presented in Menegaz et al. (2011). Their method includes one free parameter $0 < w_0 < 1$, which can be tuned to reduce prediction errors. Parameter values related to the UT, including w_0, are displayed in Table 1.

Sigma points are propagated through the model to obtain transformed points $\boldsymbol{\mathcal{L}_i} = \mathcal{F}(\boldsymbol{\mathcal{P}_i})$. In this context, the sigma points $\boldsymbol{\mathcal{P}_i}$ correspond to different time-dependent precipitation anomaly inputs, while the transformed points $\boldsymbol{\mathcal{L}_i}$ correspond to the resulting glacier length histories given those precipitation anomalies as input (Figure 4). The prior mean and covariance matrix used to generate the sigma points in Figure 4 are discussed in Sections 3.2 and 2.5.3 respectively. The sawtooth structure of

https://doi.org/10.5194/tc-2019-129
Preprint. Discussion started: 25 June 2019

the sigma points reflects the mathematical formulation of the Menegaz et al. (2011) sigma points, rather than some assumption that there is a spike in the precipitation anomaly during the Holocene.

Using the UT, we obtain the following approximation to the joint distribution

$$\begin{bmatrix} \boldsymbol{\Delta p} \\ \boldsymbol{\ell} \end{bmatrix} \sim \mathcal{N}\left(\begin{bmatrix} \mathbf{\Delta p_o} \\ \boldsymbol{\mu} \end{bmatrix}, \begin{bmatrix} P_0 & C \\ C^T & S \end{bmatrix} \right) \tag{13}$$

with

$$\boldsymbol{\mu} = \sum_{i=0}^{n} w_i \boldsymbol{\mathcal{L}_i} \tag{14}$$

$$S = \sum_{i=0}^{n} w_i (\boldsymbol{\mathcal{L}_i} - \boldsymbol{\mu})(\boldsymbol{\mathcal{L}_i} - \boldsymbol{\mu})^T + R \tag{15}$$

$$C = \sum_{i=0}^{n} w_i (\boldsymbol{\mathcal{P}_i} - \boldsymbol{\Delta p_0})(\boldsymbol{\mathcal{L}_i} - \boldsymbol{\mu})^T. \tag{16}$$

Matrices S and C are known as the measurement covariance and cross covariance respectively. Given a measurement $\boldsymbol{\ell_0}$, the joint distribution then easily yields a Gaussian approximation of the posterior distribution for $\boldsymbol{\Delta p}|\boldsymbol{\ell_0}$ (Sarkka, 2013). Letting

$$K = CS^{-1} \tag{17}$$

we have

$$\boldsymbol{\Delta p'} = \boldsymbol{\Delta p_o} + K\left[\boldsymbol{\ell_0} - \boldsymbol{\mu}\right] \tag{18}$$

$$P' = P_0 - KSK^T \tag{19}$$

$$\boldsymbol{\Delta p}|\boldsymbol{\ell_0} \sim \mathcal{N}(\boldsymbol{\Delta p'}, P'). \tag{20}$$

where $\boldsymbol{\Delta p'}$ and P' are approximations of the posterior mean and covariance respectively. Thus, $\boldsymbol{\Delta p'}$ is a discrete approximation of the optimal precipitation anomaly history. Readers familiar with the Kalman filter will recognize that $\boldsymbol{\Delta p'}$ and P' are computed using a standard Kalman update step given measurement $\boldsymbol{\ell_0}$ and Kalman gain K (Sarkka, 2013).

It is worth noting that unlike a standard filtering approach to data assimilation, all measurement data is incorporated simultaneously rather than time step by time step. For that reason, the Kalman update step corrects the entire time-dependent

https://doi.org/10.5194/tc-2019-129
Preprint. Discussion started: 25 June 2019

precipitation history at once. Moreover, unlike in Kalman smoothing, we approximate the full posterior distribution ~~rather~~ rather than the probability distributions

$$P(\Delta p_i|\boldsymbol{\ell}) \quad i = 1, \cdots, n \tag{21}$$

where $\boldsymbol{\Delta p} = [\Delta p_1, \cdots, \Delta p_n]^T$. The use of time-dependent sigma points distinguishes our approach from standard Kalman filtering or Kalman smoothing approaches.

2.5.3 Gaussian Markov Random Field Prior for Regularization

We use a Gaussian Markov random field (GMRF) prior to control the temporal smoothness of ΔP (Bardsley, 2013). The inverse covariance or precision matrix Q of the prior takes the form

$$Q = P_0^{-1} = \delta \begin{bmatrix} 2 & -1 & 0 & \cdots & 0 \\ -1 & 2 & -1 & \ddots & \vdots \\ 0 & \ddots & \ddots & \ddots & 0 \\ \vdots & \ddots & -1 & 2 & -1 \\ 0 & \cdots & 0 & -1 & 2 \end{bmatrix}. \tag{22}$$

Larger δ values produce smoother optimized solutions, whereas smaller values allow for more variation from the prior mean. We use $\delta = 5 \times 10^3$, which we find eliminates high frequency oscillations in ΔP (Secion 3).

2.5.4 Measurement Mean and Variance

Observations of terminus position are available roughly every 1000 years between 11.6 and 7.2 ka BP, with a gap from 7.2 ka BP to present. In contrast, model time steps are on the order of months. Due to these disparate time scales, we use the following procedure to estimate the measurement mean $\boldsymbol{\ell_0}$ and covariance matrix R on a time scale more appropriate for the ice sheet model.

We randomly sample curves from a multivariate Gaussian with the same covariance structure as the GMRF prior outlined in Section 2.5.3. These curves are resampled in such a way that the mean formation age and variance for each moraine approximately matches observations. The average length and variance of these curves is computed at a series of time slices to obtain a plausible measurement mean $\boldsymbol{\ell_0}$ and a diagonal measurement covariance matrix R (Figure 5).

2.5.5 Iterative Optimization Procedure

The state vector $\boldsymbol{\Delta p}$ contains values of ΔP at roughly 250 year intervals from 11.6 ka BP to present. Sparse precipitation anomaly values are linearly interpolated for input into the ice sheet model (Figure 4). Using a low temporal resolution discretization of ΔP reduces the total number of forward model runs required for the unscented transform.

https://doi.org/10.5194/tc-2019-129
Preprint. Discussion started: 25 June 2019

Optimizations are conducted in multiple passes. In the first pass, the measurement covariance matrix R is multiplied by a factor of $1/4$ so that the measurements are initially weighted more heavily than the prior. This produces a reasonable fit to the data, even given a poor initial estimate of ΔP. The optimal ΔP from a given iteration is used as the prior mean in the next iteration. We use the same prior covariance matrix P_0 for regularization in each iteration. After two to three iterations, modeled and observed terminus positions match within measurement uncertainty (Section 3). In our experience, the results of iteration are not dependent on the choice of prior mean in the first iteration, but convergence can be improved by choosing a sensible initial guess as in Section 3.2.

2.5.6 Approach to Sensitivity Testing

The data assimilation procedure can be modified to account for uncertainties in the ice flow and PDD model parameters. We define an augmented state vector

$$\boldsymbol{u} = [\boldsymbol{\Delta p}\ \boldsymbol{\theta}] \tag{23}$$

where $\boldsymbol{\theta}$ is a vector of scalar parameters including the natural logarithm the rate factor for ice, ~~basal traction~~, a parameter controlling precipitation scaling ~~with~~ temperature, and the PDD melt rate parameters for ice and snow

$$\boldsymbol{\theta} = [\ln(A),\ \beta^2,\ \lambda_p,\ \lambda_i\ ,\lambda_s]. \tag{24}$$

The prior distribution for the augmented state vector is given by

$$\boldsymbol{u} \sim \mathcal{N}\left(\begin{bmatrix}\mathbf{\Delta p_o}\\ \boldsymbol{\theta_0}\end{bmatrix}, \begin{bmatrix}P_0 & 0\\ 0 & \Theta\end{bmatrix}\right) \tag{25}$$

where $\boldsymbol{\theta_0}$ is the parameter mean vector and Θ is a diagonal matrix containing parameter variances.

The unscented transform is applied to the augmented function

$$\boldsymbol{\ell} = \hat{\mathcal{F}}(\boldsymbol{u}) + \boldsymbol{r}$$

to obtain estimates of the joint distribution for $[\boldsymbol{\Delta p}\,\boldsymbol{\theta}\,\boldsymbol{\ell}]$ and the conditional distribution for $[\boldsymbol{\Delta p}\,\boldsymbol{\theta}] \mid \boldsymbol{\ell_0}$. Since parameters are included as state variables, sigma points reflect a variety of precipitation histories and parameter sets. A model run for a particular sigma point is initialized from an appropriate steady state using the parameter set for that point.

3 Results

3.1 Reference Experiment

Here, we force the model with monthly temperatures from Buizert et al. (2018) (Figure 6 a) and a zero precipitation anomaly. Ice retreats rapidly through the Kangerlussuaq region during the early Holocene. By 10 ka BP, the terminus has retreated inland of the present day margin on both the northern and southern flowlines (Figure 6 e).

https://doi.org/10.5194/tc-2019-129
Preprint. Discussion started: 25 June 2019

3.2 Buizert Temperature Inversion

We estimate precipitation anomalies on the northern and southern flowlines using the Buizert et al. (2018) temperature reconstruction. Given the rapid retreat in the reference experiment, we expect that additional precipitation will be required in the early Holocene in order to match observed terminus positions. Therefore, in the first round of optimization, we assume a prior mean of the form

$$\Delta P = 0.5(1 - \tau) \tag{26}$$

where τ is a rescaled time variable that increases from zero at 11.6 ka BP to one at 0 ka BP. The results of the iterative optimization procedure are insensitive to the prior mean selected for the first iteration. A wide region around the mean is explored in each iteration due to the spread of the sigma points.

Positive precipitation anomalies are predicted throughout the Holocene (Figure 6 c, d). Assuming the Holocene thermal maximum extends from 10 to 6 ka BP as in Buizert et al. (2018), average HTM snowfall is 42% greater than modern on the northern flowline and 26% greater on the southern flowline (Figure 7 a). However, average snowfall during the HTM is lower than the overall Holocene average due to high precipitation from 11.6 to 10 ka BP.

3.3 Dahl-Jensen Temperature Inversion

Interpretation of the Buizert et al. (2018) temperature reconstruction is difficult due to the absence of a clear HTM. As an alternative, we estimate precipitation anomalies using the Dahl-Jensen et al. (1998) temperature reconstruction. A full Holocene temperature reconstruction is unavailable at the Dye-3 borehole site, so we use the temperature reconstruction at GRIP. The Dahl-Jensen reconstruction does not resolve seasonal temperatures. To account for this, we introduce seasonality by calculating the difference between monthly and mean annual temperatures in Buizert and adding those offsets to the mean annual temperature from Dahl-Jensen (Figure 6 b). The HTM is roughly 0.3° C warmer and 1,500 years later than indicated by Buizert et al. (2018).

Predicted precipitation anomalies are positive through most of the Holocene (Figure 6 b). Snowfall peaks during the HTM at 43% and 35% above modern on the northern and southern flowlines respectively. Average snowfall during the HTM is 25% greater than modern, whereas overall average Holocene snowfall is roughly equivalent to modern (Figure 7 b). Consequently, there is an evident relationship between HTM warming and increased snowfall.

3.4 Uncertainty Estimates during the HTM

The unscented transform is a third order accurate method for estimating the mean of a transformed Gaussian random variable, but only first order accurate for estimating covariance (Sarkka, 2013). Hence, while the unscented transform tends to be a good approximation for many nonlinear functions, it is not a full-fledged substitute for MCMC methods, which can compute expectation integrals to higher levels of accuracy. Due to this limitation, ensemble filters and the unscented Kalman filter may underestimate covariance for highly nonlinear problems (Luo and Hoteit, 2013). Practitioners will sometimes artificially

https://doi.org/10.5194/tc-2019-129
Preprint. Discussion started: 25 June 2019

inflate covariance estimates obtained from unscented or ensemble Kalman filters in order to prevent filter divergence and increase accuracy (Anderson and Anderson, 2002).

In an effort to obtain conservative uncertainty estimates, we compare the unscented transform to a higher order cubature method that is second order accurate for estimating the covariance (Appendix A). Since the fifth order method is more computationally expensive than the UT, requiring $2n^2 + 1$ sigma points for n unknown parameters, inversions are performed only on the southern flowline, and uncertainty estimates are restricted to the HTM. Model runs are initialized using the ice sheet configuration just prior to the Buizert et al. (2018) HTM obtained by forcing the model with the optimized precipitation anomaly from a previous inversion.

Mean precipitation anomaly estimates are nearly identical between the UT and fifth-order cubature methods. However, the UT appears to underestimate uncertainty during the latter half of the HTM (Figure 8). It is possible that other sigma point sets might capture the covariance structure better than the minimal sigma point from Menegaz et al. (2011). Nonetheless, the minimal sigma point set performs reasonably well considering its low computational cost.

3.5 Sensitivity Testing

We assess the sensitivity of Holocene precipitation anomalies to parameter uncertainties by performing an HTM inversion using the methodology described in Section 2.5.6. To obtain accurate uncertainty, estimates we use the 5th order cubature method. Inversions are performed on the southern flowline using the Buizert et al. (2018) temperature reconstruction. Model runs are initialized from steady states slightly before the start of the Buizert et al. (2018) HTM at 10 ka BP. Assumed parameter uncertainties are reported in Table 1.

The estimated precipitation anomaly in this experiment is within 7 cm water equivalent per year of that obtained in Section 3.4 (Figure 9). Parameter uncertainties contribute to higher uncertainty in the estimated precipitation anomaly, particularly at the beginning of the HTM. Even considering this uncertainty, the general pattern of precipitation changes is consistent with previous inversions that assumed fixed parameter values.

4 Discussion

We infer changes in Holocene precipitation in the Kangerlussuaq region of western Greenland using a new chronology of ice sheet terminus position, and inverse modeling procedure using the unscented transform. We find that a standard thermodynamic scaling of modern precipitation results in excessively fast ice retreat during the early Holocene. Precipitation inversions using both the Buizert et al. (2018) and Dahl-Jensen et al. (1998) temperature reconstructions indicate that additional precipitation is required to match the observed retreat history in the region. However, the timing of the Holocene thermal maximum (HTM) and the predicted precipitation histories differ between the two temperature reconstructions.

Inversions using the Buizert et al. (2018) temperature reconstruction predict elevated snowfall throughout the Holocene. Average HTM snowfall is around 30% greater than modern. Due to high snowfall in the early Holocene (nearly 100% higher than modern) and a dip in HTM precipitation associated with the 8.2 ka BP cold event, the HTM average nearly matches the

https://doi.org/10.5194/tc-2019-129
Preprint. Discussion started: 25 June 2019

overall Holocene average. In contrast, inversions using the Dahl-Jensen temperature reconstruction show a clear trend between HTM warming and increased precipitation. HTM snowfall is around 25% higher than the Holocene average.

Differences in the Buizert et al. (2018) and Dahl-Jensen et al. (1998) temperature reconstructions result in inconsistencies in estimated precipitation anomalies. In the Buizert et al. (2018) reconstruction, mean annual temperature increases rapidly from 11.6 to 10 ka BP. Rapid warming results in high predicted snowfall, stabilizing the ice sheet during a period of relatively slow retreat from 11.6 to 10.3 ka BP. High snowfall in the early Holocene significantly influences the overall Holocene average. Temperatures increase more gradually in the Dahl-Jensen et al. (1998) temperature reconstruction, and precipitation anomalies are therefore low at the onset of the Holocene.

Estimated precipitation anomalies during the HTM are not particularly sensitive to uncertainties in the ice sheet or PDD model parameters, or to the initialization procedure ~~(Figure 9).~~ In the sensitivity test in Section 2.5.6, model runs are initialized using one of a set of several steady states using different parameter combinations. In Section 3.4, which compares the UT to a fifth order cubature method, model runs are initialized from a single transient ice sheet state using output from a previous inversion. Despite these differences in model initialization, and the effects of parameter uncertainties, estimated HTM precipitation anomalies are comparable in both inversions.

Unexpectedly, using the Dahl-Jensen et al. (1998) reconstruction results in a non-zero precipitation anomaly at 0 ka BP. Aside from the distance of GRIP from Kangerlussuaq (over 500 km,) a possible explanation for this feature is that the Dahl-Jensen et al. (1998) reconstruction is obtained by inverting for surface temperatures given an ice core temperature profile. Ice core temperatures carry a diffuse record of surface temperature, with greater uncertainty earlier in time. These uncertanties may alter the inverted precipitation history. Moreoever, ice sheet terminus position may respond to changes in temperature and precipitation on a shorter timescale than can be resolved using borehole temperature data alone (Lesnek and Briner, 2018; Young et al., 2019, In Review; Winsor et al., 2015).

4.1 Conclusions

4.1.1 The Unscented Transform as a Data Assimilation Method

Significant strides have been made in time-dependent data assimilation in glaciology using adjoint based methods. Goldberg and Heimbach (2013) infer the initial thickness and basal conditions for a synthetic ice sheet given snapshots of ice thickness at discrete times. Larour et al. (2014) demonstrate a data assimilation framework within the Ice Sheet System Model (ISSM), capable of obtaining temporal estimates of surface mass balance and basal friction given surface altimetry.

In contrast to these adjoint based approaches, the unscented transform does not require computing the Jacobian or Hessian of an objective function, or special checkpointing code for time-dependent problems. Adjoint based methods are advantageous for extremely high-dimensional problems, as the required number of model runs is independent of the number of parameters. However, the UT provides more accurate uncertainty estimates than linearization (Julier and Uhlmann, 1997). Hessian information can be used to improve uncertainty estimates (Isaac et al., 2015), but to our knowledge, this approach has not been applied to time-dependent problems in glaciology.

https://doi.org/10.5194/tc-2019-129
Preprint. Discussion started: 25 June 2019

The unscented transform also has significant advantages over Markov chain Monte Carlo methods for some problems. Since function evaluations at each sigma point are independent, the UT is trivially parallelizable. MCMC methods can be parallelized to some extent by utilizing multiple interacting Markov chains running in parallel (e.g. Chowdhury and Jermaine, 2018) or by combining samples from independent chains in a post processing step (e.g. Neiswanger et al., 2013). Nonetheless, computational bottlenecks persist in MCMC methods since individual Markov chains are inherently serial.

The potential accuracy of the unscented transform is limited since it uses a predetermined number of points. In our case, using a minimal set of $n+1$ sigma points for n unknown parameters yields accurate mean estimates but appears to underestimate covariance when compared to a higher order cubature method (Figure 7). MCMC methods can provide more accurate estimates given sufficient computation time. In theory, MCMC methods are more viable than the UT for extremely high dimensional problems since their convergence rate is independent of dimension. In practice, however, the number of function evaluations needed for MCMC methods makes them intractable for some problems.

4.1.2 Modeling Conclusions

Our work follows a number of previous observationally constrained paleo ice sheet modeling studies (e.g. Tarasov and Peltier, 2002; Lecavalier et al., 2014; Calov et al., 2015). Perhaps most relevant to this work is Lecavalier et al. (2014), who model the deglaciation of Greenland from the Last Glacial Maximum using a 3-D thermomechanically coupled ice sheet model. Model runs in Lecavalier et al. (2014) are informed by constraints on relative sea level, ice core thinning, and LGM ice sheet extent.

In contrast to previous modeling studies, the computational efficiency of the flowline model outlined in Brinkerhoff et al. (2017) makes time-dependent data-assimilation, sensitivity testing, and robust uncertainty estimation tractable. Sensitivity tests indicate that precipitation anomaly inversions are consistent when accounting for parameter uncertainties in the ice-dynamics model. This result supports earlier findings showing that modeled Holocene retreat in land terminating regions is more sensitive to surface mass balance than other factors like the flow law or basal sliding (Cuzzone et al., 2019; Lecavalier et al., 2014).

A drawback of our modeling approach is that we cannot account for inherently map plane effects like changes in ice flow direction, or convergent and divergent flow in or out of the modeled flow path. These factors likely contribute to discrepancies in estimated precipitation anomalies between the northern and southern flowlines (Figure 6). Precipitation anomalies are also highly sensitive to the temperature forcing, which introduces another source of uncertainty. In this work, we have not treated temperature as a random variable with its own covariance structure. However, differences in the Buizert et al. (2018) and Dahl-Jensen et al. (1998) temperature reconstructions suggest the effect of temperature uncertainties on estimated precipitation anomalies can be pronounced. This result underscores the importance of generating improved temperature reconstructions constrained by proxy records.

Despite lingering uncertainties, our modeling results support our hypothesis that the Holocene thermal maximum was accompanied by greater than modern precipitation, which reduced the rate of retreat through the Kangerlussuaq region. Forcing the model with estimated precipitation anomalies results in a plausible retreat history on both paleo-flowlines (Figure 6 e, f). Arctic warming and changing sea ice extent are expected to cause similar changes in precipitation that will influence future GrIS mass balance. According to Bintanja and Selten (2014), declining sea ice may cause an increase in net accumulation

https://doi.org/10.5194/tc-2019-129
Preprint. Discussion started: 25 June 2019

over areas of Arctic land ice. Similarly, Singarayer et al. (2006) link increased Arctic warming and sea-ice decline to increased precipitation, projecting precipitation will increase by more than 50% by the end of the century.

Code availability. The flowline ice sheet model and PDD model used in this work are available at https://github.com/JacobDowns/flow_model.

Appendix A: A Higher Order Method for Estimating Covariance

Estimating the mean and covariance of the posterior distribution requires approximating Gaussian weighted expectation integrals of the form

$$E[\mathcal{F}(\boldsymbol{x})] = \int_{\mathbb{R}^n} \mathcal{F}(\boldsymbol{x})\mathcal{N}(\mathbf{0}, I)\, d\boldsymbol{x} \tag{A1}$$

via numerical integratation rules, also called cubature rules, which approximate the expectation integral as a weighted sum

$$E[\mathcal{F}(\boldsymbol{x})] \approx Q[\mathcal{F}(\boldsymbol{x})] = \sum_{i=1}^{N} w_i \mathcal{F}(\boldsymbol{\chi_i}). \tag{A2}$$

General Gaussian weight functions $\mathcal{N}(\boldsymbol{x_0}, P_x)$ are handled by changing variables. Letting $\sqrt{P_x}$ be a matrix square root of the covariance matrix, we have

$$\begin{aligned} &\int_{\mathbb{R}^n} \mathcal{F}(\boldsymbol{x})\mathcal{N}(\boldsymbol{x_0}, P_x)\, d\boldsymbol{x} \\ &= \int_{\mathbb{R}^n} \mathcal{F}(\boldsymbol{x_0} + \sqrt{P_x}\,\boldsymbol{\xi})\mathcal{N}(\mathbf{0}, I)\, d\boldsymbol{\xi}. \end{aligned} \tag{A3}$$

Cubature rules, including the unscented transform, are constructed to exactly integrate polynomial functions $\mathcal{F}(\boldsymbol{x})$ up to a certain degree d. Suppose that $\boldsymbol{x} = [x_1, x_2, \cdots, x_n]^T$ is a point in $\mathbb{R}^n$. A monomial of degree d refers to a function $x_1^{i_1} x_2^{i_2} \cdots x_n^{i_n}$ where the exponents are non-negative integers that sum to d. A polynomial of degree d is a linear combination of monomials with highest degree d.

Li et al. (2017) describe a fifth-order cubature rule using fully symmetric sets of sigma points. A set $X = \{\boldsymbol{\chi_1}, \boldsymbol{\chi_2}, \cdots, \boldsymbol{\chi_N}\}$ is fully symmetric if it is closed under the operations of coordinate position and sign permutations. Their cubature rule has the form

$$\begin{aligned} Q[\mathcal{F}(\boldsymbol{x})] &= w_1 \mathcal{F}(0, 0, \cdots, 0) \\ &+ w_2 \sum_{\text{full sym}} \mathcal{F}(\lambda, 0, \cdots, 0) \\ &+ w_3 \sum_{\text{full sym}} \mathcal{F}(\lambda, \lambda, 0, \cdots, 0). \end{aligned} \tag{A4}$$

https://doi.org/10.5194/tc-2019-129
Preprint. Discussion started: 25 June 2019


The Cryosphere Discussions

The notation $\sum_{\text{full sym}} \mathcal{F}(\cdot)$ refers to a sum of the function $\mathcal{F}$ evaluated at all points in the fully symmetric set generated by the given point.

Due to the symmetry of the sigma points and the Gaussian weight function, all moments (that is, integrals of Gaussian weighted monomial functions) containing an odd order exponent are automatically satisfied. Exploiting this fact, and the symmetries of the sigma points, it can be shown that satisfying the remaining moment constraint equations up the fifth order reduces to solving the following system of four equations in four unknowns w_1, w_2, w_3 and λ

$$\begin{aligned} E[1] &= w_1 + 2nw_2 + 2n(n-1)w_3 \\ E[x_i^2] &= 2\lambda^2 w_2 + 4(n-1)\lambda^2 w_3 \\ E[x_i^4] &= 2\lambda^4 w_2 + 4(n-1)\lambda^4 w_3 \\ E[x_i^2 x_j^2] &= 4\lambda^4 w_3. \end{aligned} \tag{A5}$$

By slightly modifying this cubature rule

$$\begin{aligned} Q[\mathcal{F}(\boldsymbol{x})] &= w_1 \mathcal{F}(0,0,\cdots,0) \\ &+ w_2 \sum_{\text{full sym}} \mathcal{F}(\lambda_1,0,\cdots,0) \\ &+ w_3 \sum_{\text{full sym}} \mathcal{F}(\lambda_2,\lambda_2,0,\cdots,0) \end{aligned} \tag{A6}$$

we introduce a new free parameter λ_2 that allows scaling of the sigma points about the mean. The new moment constraint equations become

$$\begin{aligned} E[1] &= w_1 + 2nw_2 + 2n(n-1)w_3 \\ E[x_i^2] &= 2\lambda_1^2 w_2 + 4(n-1)\lambda_2^2 w_3 \\ E[x_i^4] &= 2\lambda_1^4 w_2 + 4(n-1)\lambda_2^4 w_3 \\ E[x_i^2 x_j^2] &= 4\lambda_2^4 w_3. \end{aligned} \tag{A7}$$

Using that $E[1] = 1$, $E[x_i^2] = 1$, $E[x_i^4] = 3$, and $E[x_i^2 x_j^2] = 1$ we obtain

$$\begin{aligned} \lambda_1 &= \frac{\lambda_2\sqrt{n-4}}{n-\lambda_2^2-1} \\ w_2 &= \frac{4-n}{2\lambda_1^4} \\ w_3 &= \frac{1}{4\lambda_2^2} \\ w_1 &= 1 - 2nw_2 - 2n(n-1)w_3 \end{aligned} \tag{A8}$$

with $n > 4$ and $n - \lambda_2^2 - 1 \neq 0$. A drawback of the original cubature rule, as well the modification of it presented here, is that it requires negative weights, which can lead to numerical instability.

https://doi.org/10.5194/tc-2019-129
Preprint. Discussion started: 25 June 2019

Author contributions. JD was the lead author of this manuscript. JJ and JC assisted JD with ice sheet modeling efforts. JB, NY, and AL provided the moraine age data used in this work. JD and JJ wrote the manuscript with input from all authors.

Competing interests. The authors declare that they have no conflict of interest.

Acknowledgements. JD and JJ were supported by NSF grant 1504457. JD would like to thank Doug Brinkerhoff for providing code for the flowline ice sheet model used in this work, as well as many elucidating discussions.

https://doi.org/10.5194/tc-2019-129
Preprint. Discussion started: 25 June 2019

References

Alley, R. B., Meese, D. A., Shuman, C. A., Gow, A. J., Taylor, K. C., Grootes, P. M., White, J. W., Ram, M., Waddington, E. D., Mayewski, P. A., and Zielinski, G. A.: Abrupt increase in Greenland snow accumulation at the end of the Younger Dryas event, Nature, https://doi.org/10.1038/362527a0, 1993.

Anderson, J. L. and Anderson, S. L.: A Monte Carlo Implementation of the Nonlinear Filtering Problem to Produce Ensemble Assimilations and Forecasts, Monthly Weather Review, https://doi.org/10.1175/1520-0493(1999)127<2741:amciot>2.0.co;2, 2002.

Bardsley, J. M.: Gaussian markov random field priors for inverse problems, Inverse Problems and Imaging, https://doi.org/10.3934/ipi.2013.7.397, 2013.

Bintanja, R. and Selten, F. M.: Future increases in Arctic precipitation linked to local evaporation and sea-ice retreat, Nature, https://doi.org/10.1038/nature13259, 2014.

Blatter, H.: Velocity and stress fields in grounded glaciers: a simple algorithm for including deviatoric stress gradients, Journal of Glaciology, https://doi.org/10.1017/S002214300001621X, 1995.

Box, J. E.: Greenland ice sheet mass balance reconstruction. Part II: Surface mass balance (1840-2010), Journal of Climate, https://doi.org/10.1175/JCLI-D-12-00518.1, 2013.

Brinkerhoff, D., Truffer, M., and Aschwanden, A.: Sediment transport drives tidewater glacier periodicity, Nature Communications, https://doi.org/10.1038/s41467-017-00095-5, 2017.

Buizert, C., Keisling, B. A., Box, J. E., He, F., Carlson, A. E., Sinclair, G., and DeConto, R. M.: Greenland-Wide Seasonal Temperatures During the Last Deglaciation, Geophysical Research Letters, https://doi.org/10.1002/2017GL075601, 2018.

Calov, R., Robinson, A., Perrette, M., and Ganopolski, A.: Simulating the Greenland ice sheet under present-day and palaeo constraints including a new discharge parameterization, Cryosphere, https://doi.org/10.5194/tc-9-179-2015, 2015.

Caron, L., Ivins, E. R., Larour, E., Adhikari, S., Nilsson, J., and Blewitt, G.: GIA Model Statistics for GRACE Hydrology, Cryosphere, and Ocean Science, Geophysical Research Letters, https://doi.org/10.1002/2017GL076644, 2018.

Chib, S. and Greenberg, E.: Understanding the metropolis-hastings algorithm, American Statistician, https://doi.org/10.1080/00031305.1995.10476177, 1995.

Chowdhury, A. and Jermaine, C.: Parallel and Distributed MCMC via Shepherding Distributions, Proceedings of the Twenty-First International Conference on Artificial Intelligence and Statistics, 84, 1819–1827, http://proceedings.mlr.press/v84/chowdhury18a.html, 2018.

Cuzzone, J. K., Schlegel, N. J., Morlighem, M., Larour, E., Briner, J. P., Seroussi, H., and Caron, L.: The impact of model resolution on the simulated Holocene retreat of the southwestern Greenland ice sheet using the Ice Sheet System Model (ISSM), Cryosphere, https://doi.org/10.5194/tc-13-879-2019, 2019.

Dahl-Jensen, D., Mosegaard, K., Gundestrup, N., Clow, G. D., Johnsen, S. J., Hansen, A. W., and Balling, N.: Past temperatures directly from the Greenland Ice Sheet, Science, https://doi.org/10.1126/science.282.5387.268, 1998.

Goldberg, D. N. and Heimbach, P.: Parameter and state estimation with a time-dependent adjoint marine ice sheet model, Cryosphere, https://doi.org/10.5194/tc-7-1659-2013, 2013.

Isaac, T., Petra, N., Stadler, G., and Ghattas, O.: Scalable and efficient algorithms for the propagation of uncertainty from data through inference to prediction for large-scale problems, with application to flow of the Antarctic ice sheet, Journal of Computational Physics, https://doi.org/10.1016/j.jcp.2015.04.047, 2015.

Johannesson, T., Sigurdsson, O., Laumann, T., and Kennett, M.: Degree-day glacier mass-balance modelling with applications to glaciers in Iceland, Norway and Greenland, Journal of Glaciology, https://doi.org/10.1017/S0022143000016221, 1995.

Julier, S. J. and Uhlmann, J. K.: New extension of the Kalman filter to nonlinear systems, Int Symp AerospaceDefense Sensing Simul and Controls, https://doi.org/10.1117/12.280797, 1997.

Kaufman, D. S., Ager, T. A., Anderson, N. J., Anderson, P. M., Andrews, J. T., Bartlein, P. J., Brubaker, L. B., Coats, L. L., Cwynar, L. C., Duvall, M. L., Dyke, A. S., Edwards, M. E., Eisner, W. R., Gajewski, K., Geirsdóttir, A., Hu, F. S., Jennings, A. E., Kaplan, M. R., Kerwin, M. W., Lozhkin, A. V., MacDonald, G. M., Miller, G. H., Mock, C. J., Oswald, W. W., Otto-Bliesner, B. L., Porinchu, D. F., Rühland, K., Smol, J. P., Steig, E. J., and Wolfe, B. B.: Holocene thermal maximum in the western Arctic (0-180°W), Quaternary Science Reviews, https://doi.org/10.1016/j.quascirev.2003.09.007, 2004.

Kobashi, T., Menviel, L., Jeltsch-Thömmes, A., Vinther, B. M., Box, J. E., Muscheler, R., Nakaegawa, T., Pfister, P. L., Döring, M., Leuenberger, M., Wanner, H., and Ohmura, A.: Volcanic influence on centennial to millennial Holocene Greenland temperature change, Scientific Reports, https://doi.org/10.1038/s41598-017-01451-7, 2017.

Larour, E., Utke, J., Csatho, B., Schenk, A., Seroussi, H., Morlighem, M., Rignot, E., Schlegel, N., and Khazendar, A.: Inferred basal friction and surface mass balance of the Northeast Greenland Ice Stream using data assimilation of ICESat (Ice Cloud and land Elevation Satellite) surface altimetry and ISSM (Ice Sheet System Model), Cryosphere, https://doi.org/10.5194/tc-8-2335-2014, 2014.

Lecavalier, B. S., Milne, G. A., Simpson, M. J., Wake, L., Huybrechts, P., Tarasov, L., Kjeldsen, K. K., Funder, S., Long, A. J., Woodroffe, S., Dyke, A. S., and Larsen, N. K.: A model of Greenland ice sheet deglaciation constrained by observations of relative sea level and ice extent, Quaternary Science Reviews, 102, 54–84, https://doi.org/10.1016/j.quascirev.2014.07.018, 2014.

Lesnek, A. J. and Briner, J. P.: Response of a land-terminating sector of the western Greenland Ice Sheet to early Holocene climate change: Evidence from10Be dating in the Søndre Isortoq region, Quaternary Science Reviews, https://doi.org/10.1016/j.quascirev.2017.11.028, 2018.

Li, Z., Yang, W., Ding, D., and Liao, Y.: A Novel Fifth-Degree Cubature Kalman Filter for Real-Time Orbit Determination by Radar, Mathematical Problems in Engineering, https://doi.org/10.1155/2017/8526804, 2017.

Luo, X. and Hoteit, I.: Covariance Inflation in the Ensemble Kalman Filter: A Residual Nudging Perspective and Some Implications, Monthly Weather Review, https://doi.org/10.1175/mwr-d-13-00067.1, 2013.

Marcott, S. A., Shakun, J. D., Clark, P. U., and Mix, A. C.: A reconstruction of regional and global temperature for the past 11,300 years, Science, 339, 1198–1201, https://doi.org/10.1126/science.1228026, 2013.

Menegaz, H. M., Ishihara, J. Y., and Borges, G. A.: A new smallest sigma set for the Unscented Transform and its applications on SLAM, in: Proceedings of the IEEE Conference on Decision and Control, https://doi.org/10.1109/CDC.2011.6161480, 2011.

Miller, G. H., Brigham-Grette, J., Alley, R. B., Anderson, L., Bauch, H. A., Douglas, M. S., Edwards, M. E., Elias, S. A., Finney, B. P., Fitzpatrick, J. J., Funder, S. V., Herbert, T. D., Hinzman, L. D., Kaufman, D. S., MacDonald, G. M., Polyak, L., Robock, A., Serreze, M. C., Smol, J. P., Spielhagen, R., White, J. W., Wolfe, A. P., and Wolff, E. W.: Temperature and precipitation history of the Arctic, Quaternary Science Reviews, https://doi.org/10.1016/j.quascirev.2010.03.001, 2010.

Morlighem, M., Williams, C. N., Rignot, E., An, L., Arndt, J. E., Bamber, J. L., Catania, G., Chauché, N., Dowdeswell, J. A., Dorschel, B., Fenty, I., Hogan, K., Howat, I., Hubbard, A., Jakobsson, M., Jordan, T. M., Kjeldsen, K. K., Millan, R., Mayer, L., Mouginot, J., Noël, B. P., O'Cofaigh, C., Palmer, S., Rysgaard, S., Seroussi, H., Siegert, M. J., Slabon, P., Straneo, F., van den Broeke, M. R., Weinrebe, W., Wood, M., and Zinglersen, K. B.: BedMachine v3: Complete Bed Topography and Ocean Bathymetry Mapping of Greenland From

Multibeam Echo Sounding Combined With Mass Conservation, Geophysical Research Letters, https://doi.org/10.1002/2017GL074954, 2017.

Mouginot, J., Rignot, E., Scheuchl, B., and Millan, R.: Comprehensive annual ice sheet velocity mapping using Landsat-8, Sentinel-1, and RADARSAT-2 data, Remote Sensing, https://doi.org/10.3390/rs9040364, 2017.

Neiswanger, W., Wang, C., and Xing, E.: Asymptotically Exact, Embarrassingly Parallel MCMC, Proceeding UAI'14 Proceedings of the Thirtieth Conference on Uncertainty in Artificial Intelligence, pp. 1–16, http://arxiv.org/abs/1311.4780, 2013.

Pattyn, F.: A new three-dimensional higher-order thermomechanical ice sheet model: Basic sensitivity, ice stream development, and ice flow across subglacial lakes, Journal of Geophysical Research, https://doi.org/10.1029/2002JB002329, 2003.

Polyak, L., Alley, R. B., Andrews, J. T., Brigham-Grette, J., Cronin, T. M., Darby, D. A., Dyke, A. S., Fitzpatrick, J. J., Funder, S., Holland, M., Jennings, A. E., Miller, G. H., O'Regan, M., Savelle, J., Serreze, M., St. John, K., White, J. W., and Wolff, E.: History of sea ice in the Arctic, Quaternary Science Reviews, https://doi.org/10.1016/j.quascirev.2010.02.010, 2010.

Reeh, N.: Parameterization of Melt Rate and Surface Temperature on the Greenland Ice Sheet, Polarforschung, https://doi.org/10.1007/978-3-7091-0973-1_2, 1991.

Ritz, C., Rommelaere, V., and Dumas, C.: Modeling the evolution of Antarctic ice sheet over the last 420,000 years: Implications for altitude changes in the Vostok region, Journal of Geophysical Research Atmospheres, https://doi.org/10.1029/2001JD900232, 2001.

Sarkka, S.: Bayesian Filtering and Smoothing, Cambridge University Press, https://doi.org/10.1017/CBO9781139344203, 2013.

Singarayer, J. S., Bamber, J. L., and Valdes, P. J.: Twenty-first-century climate impacts from a declining Arctic sea ice cover, Journal of Climate, https://doi.org/10.1175/JCLI3649.1, 2006.

Tarasov, L. and Peltier, W. R.: Greenland glacial history and local geodynamic consequences, Geophysical Journal International, https://doi.org/10.1046/j.1365-246X.2002.01702.x, 2002.

Thomas, E. K., Briner, J. P., Ryan-Henry, J. J., and Huang, Y.: A major increase in winter snowfall during the middle Holocene on western Greenland caused by reduced sea ice in Baffin Bay and the Labrador Sea, Geophysical Research Letters, https://doi.org/10.1002/2016GL068513, 2016.

Winsor, K., Carlson, A. E., Caffee, M. W., and Rood, D. H.: Rapid last-deglacial thinning and retreat of the marine-terminating southwestern Greenland ice sheet, Earth and Planetary Science Letters, 426, 1–12, https://doi.org/10.1016/j.epsl.2015.05.040, 2015.

Young, N. E., Briner, J. P., Miller, G. H., Crump, S. E., Lesnek, A. J., and Thomas, E. K.: Arctic deglaciation interrupted by abrupt coolings, Science Advances, 2019, In Review.

https://doi.org/10.5194/tc-2019-129
Preprint. Discussion started: 25 June 2019

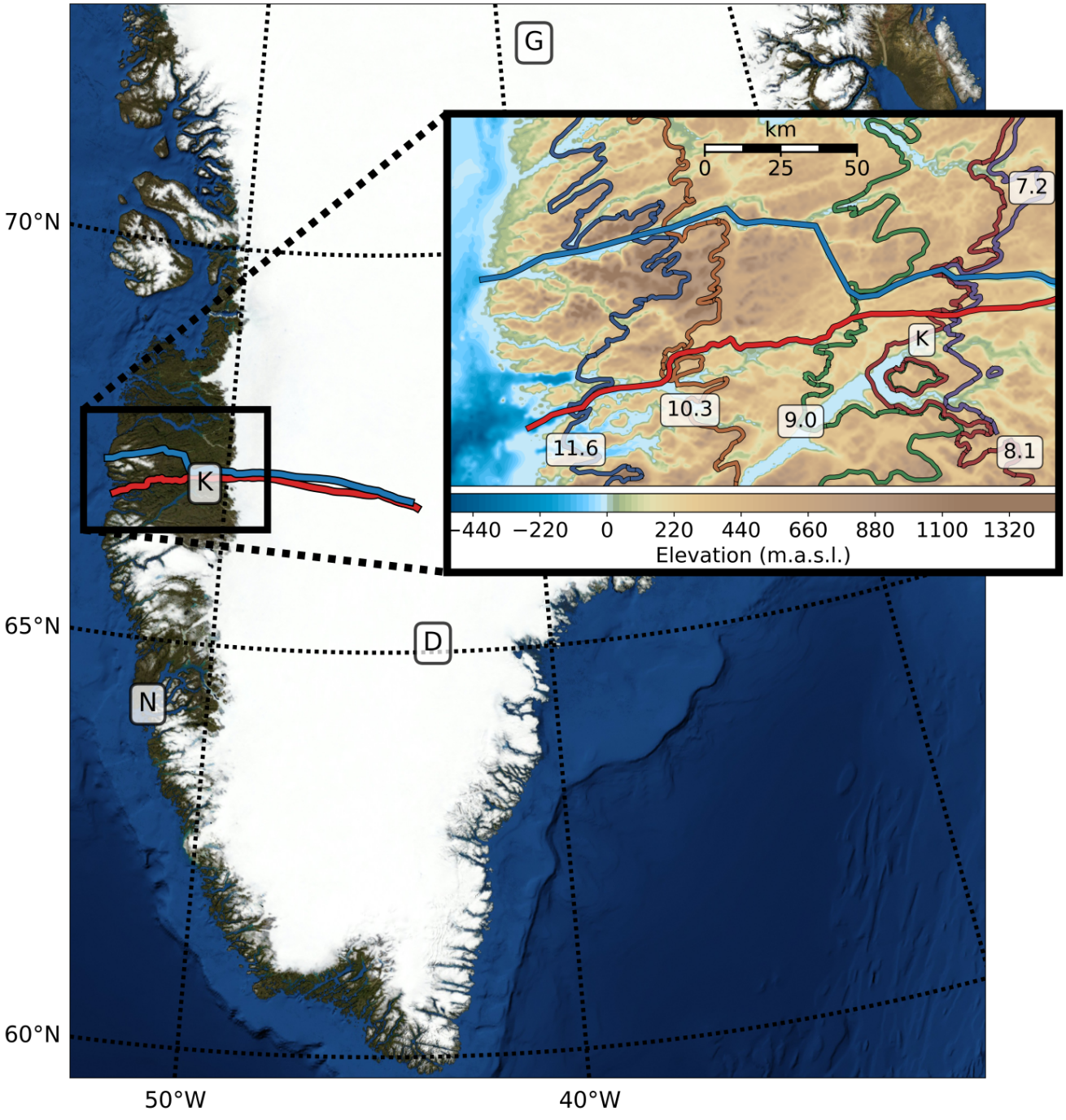

Figure 1. Bedrock geometry in the Kangerlussuaq region of western Greenland in meters above sea level. K and N mark the locations of Kangerlussuaq and Nuuk respectively. D and G mark the locations of the Dye-3 and GISP2 boreholes respectively. Northern and southern paleo-flowlines are shown as blue and red lines running left to right. Historical moraines dating from 11.6 to 7.2 ka BP are shown as colored lines.

https://doi.org/10.5194/tc-2019-129
Preprint. Discussion started: 25 June 2019

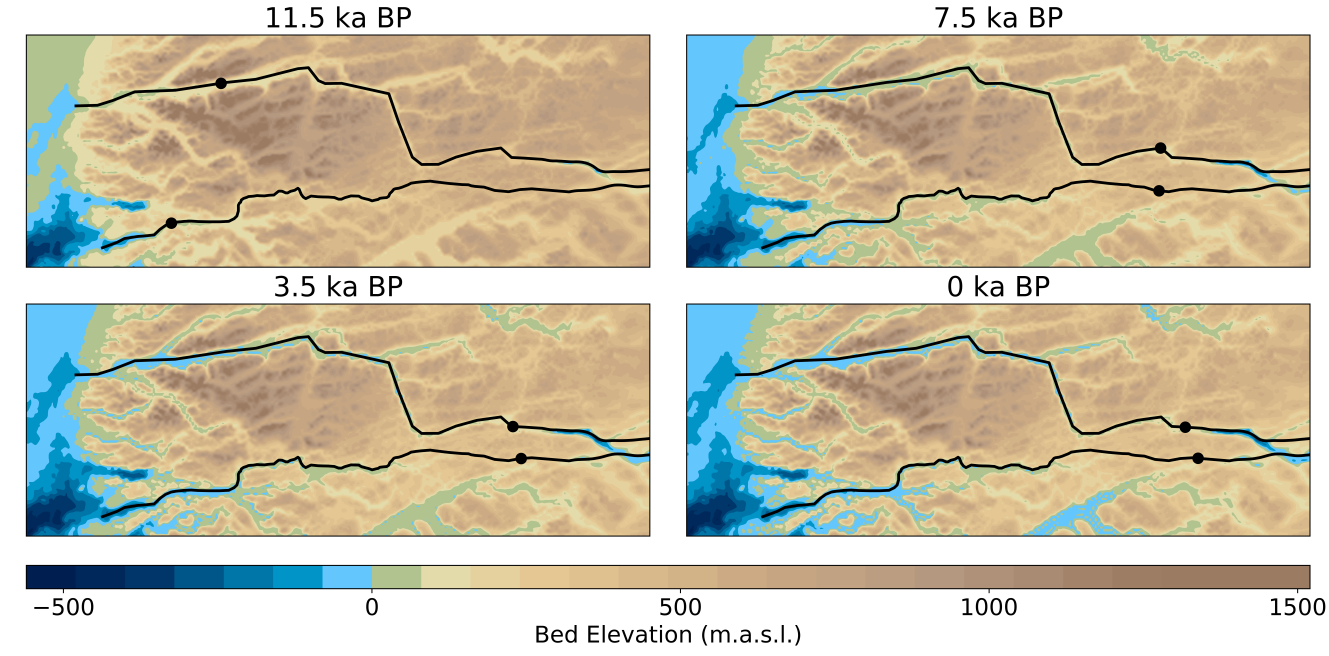

Figure 2. Bedrock elevation and sea level changes in the Kangerlussuaq region from 11.5 ka BP to modern. Paleo-flowlines are shown in black. Approximate terminus positions during each time period are indicated by black dots.

https://doi.org/10.5194/tc-2019-129
Preprint. Discussion started: 25 June 2019

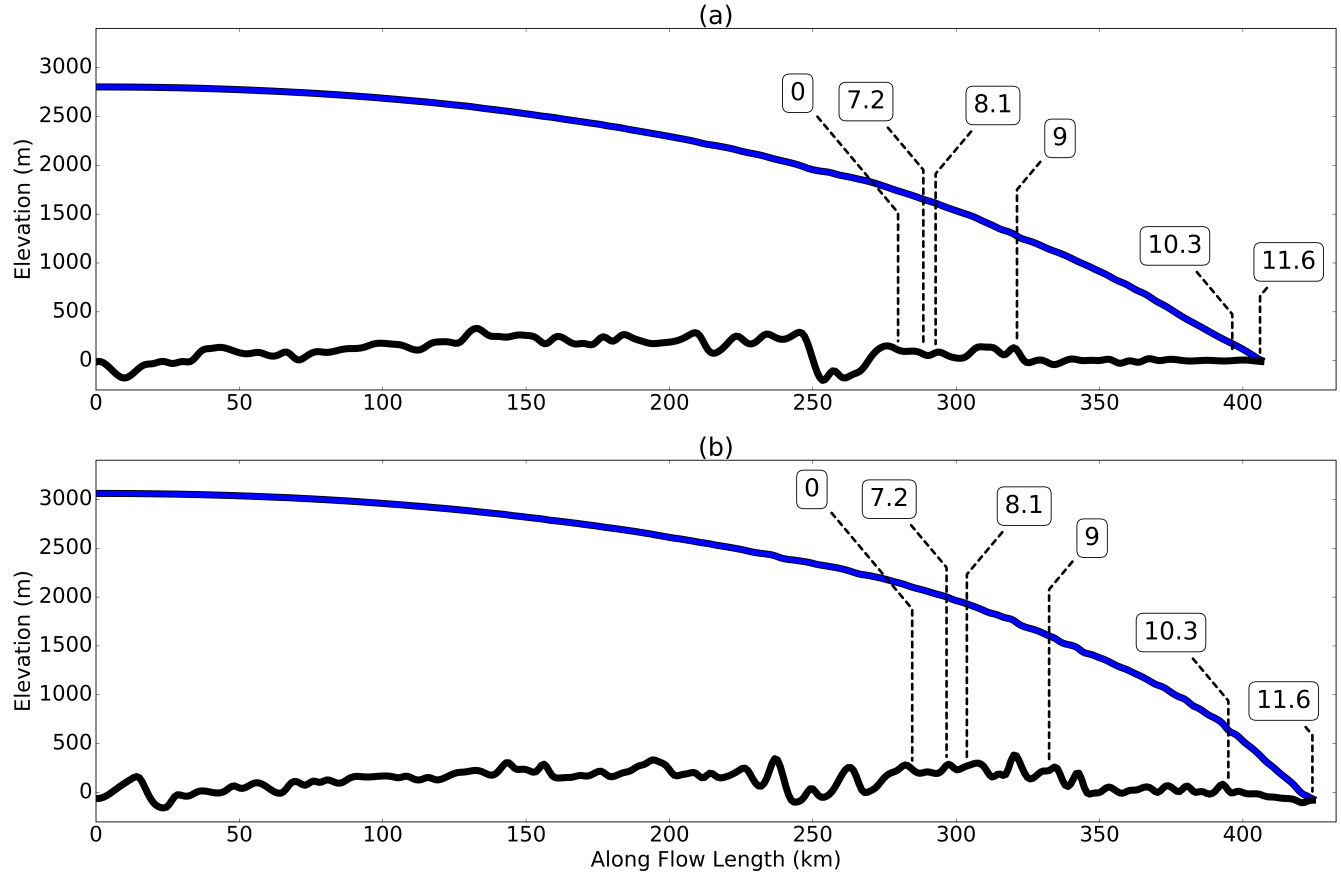

Figure 3. Steady state ice sheet configurations for the northern (a) and southern (b) paleo-flowlines. Solid black and blue lines represent the bedrock elevation and ice surface respectively. Moraine positions are shown with dashed lines, with associated ages expressed in thousands of years before present.

https://doi.org/10.5194/tc-2019-129
Preprint. Discussion started: 25 June 2019

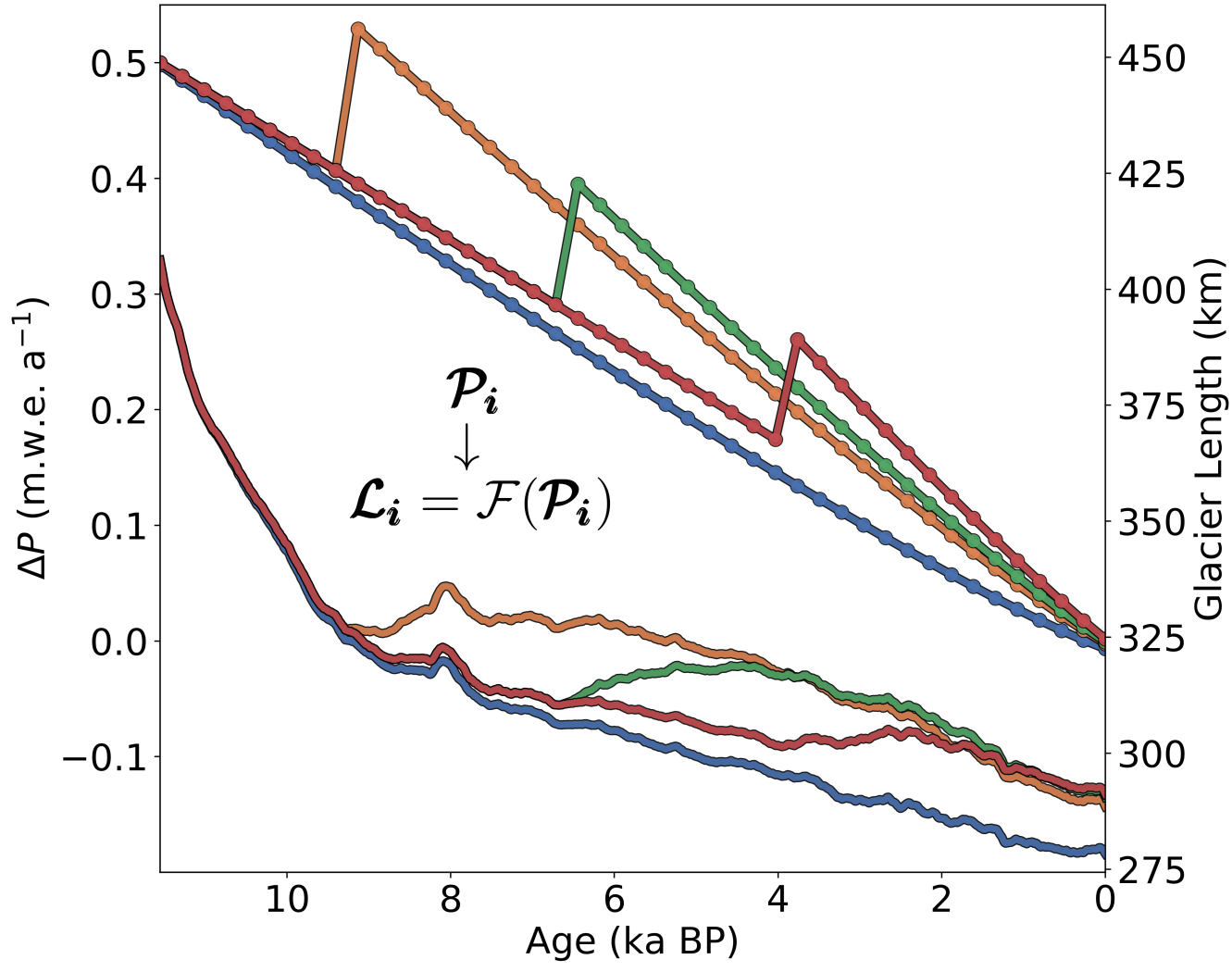

Figure 4. Transformation of a subset of sigma points $\boldsymbol{\mathcal{P}_i}$ (circles connected by lines), which correspond to different precipitation anomaly inputs, into transformed points $\boldsymbol{\mathcal{L}_i}$ (solid lines), which give the resulting glacier length histories obtained from the ice sheet model $\mathcal{F}$.

https://doi.org/10.5194/tc-2019-129
Preprint. Discussion started: 25 June 2019

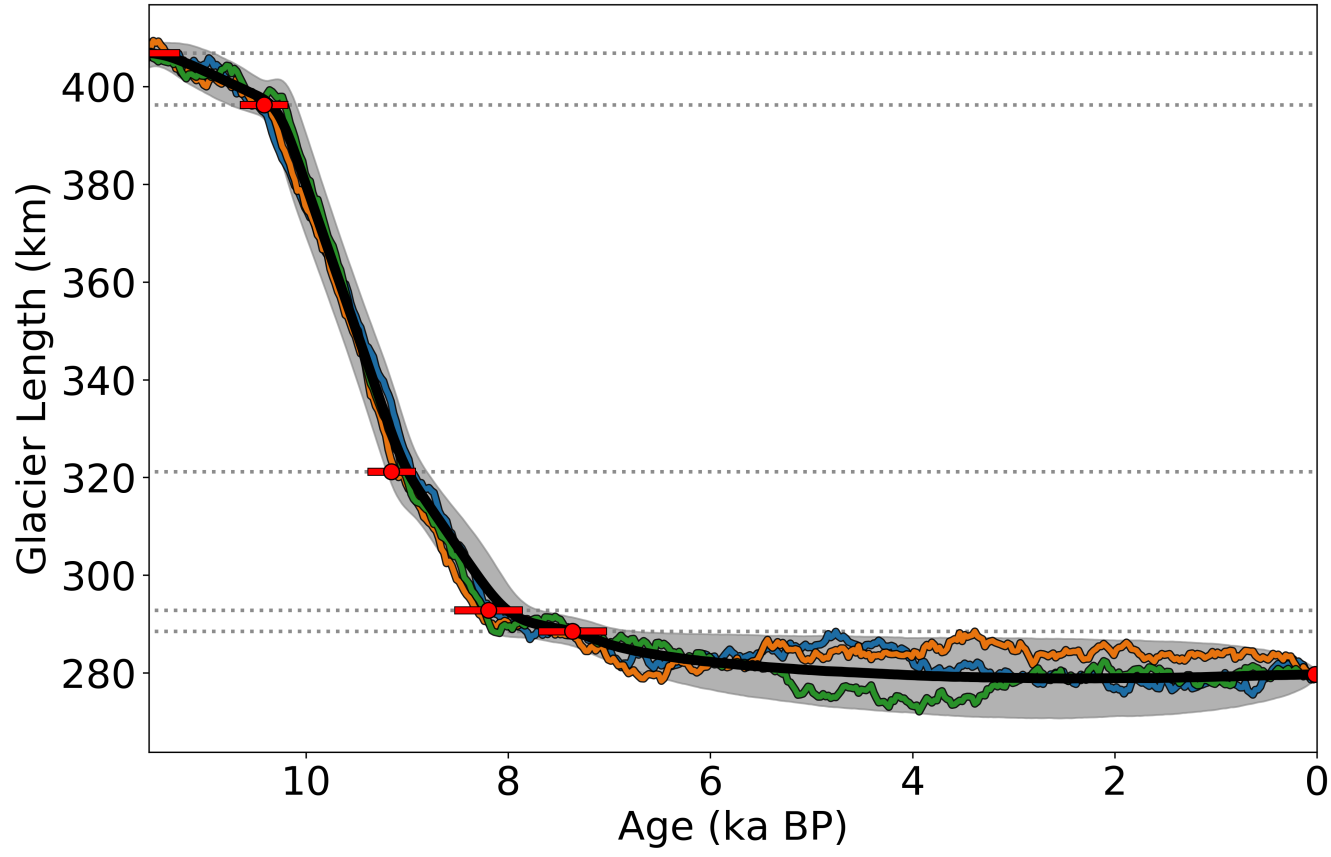

Figure 5. The measurement mean ℓ_0 (solid black line) and 95% confidence bands (gray shaded region) for the northern flowline are estimated by generating random curves (e.g. the green, blue, and orange lines) with the same mean moraine formation ages and variances as the observations. Red dots denote the estimated mean moraine formation ages, while red lines show 95% confidence intervals.

https://doi.org/10.5194/tc-2019-129
Preprint. Discussion started: 25 June 2019

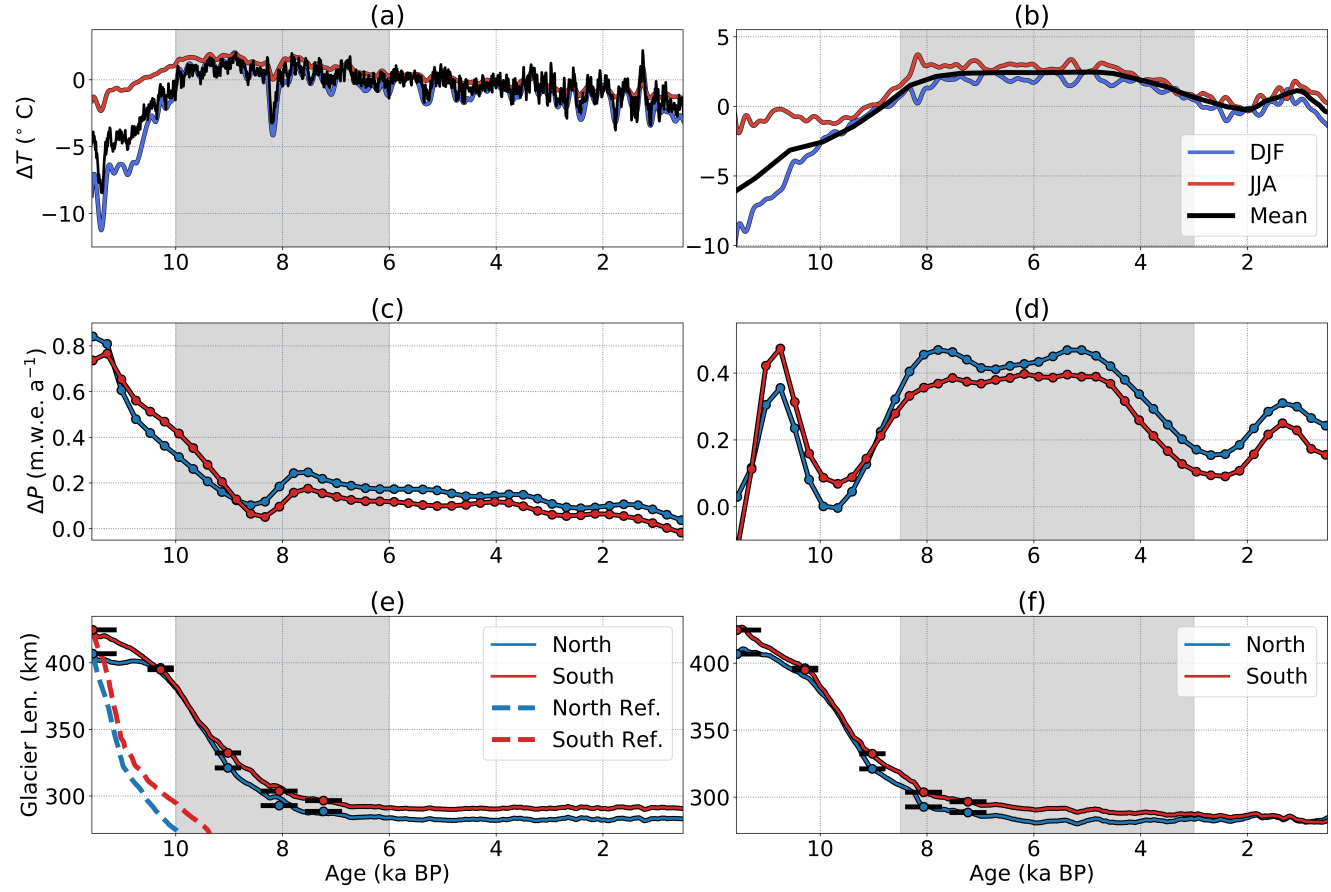

Figure 6. Buizert et al. (2018) and Dahl-Jensen et al. (1998) temperature anomalies are displayed in (a) and (b) respectively. Black lines show mean annual temperature anomalies, blue lines show December, January, February averages, and red lines show June, July, August averages. The HTM for each temperature record is shaded gray. Panels (c) and (d) show estimated precipitation anomalies on both flowlines for the Buizert and Dahl-Jensen temperature reconstructions respectively. Modeled terminus positions obtained from using the estimated precipitation anomalies for Buizert and Dahl-Jensen temperature inversions are shown in (e) and (f) respectively. Observed terminus positions and 95% uncertainty intervals are indicated by colored points and black lines. The dashed lines in panel (e) show modeled terminus positions for both flowlines using the Buizert temperature reconstruction and a zero precipitation anomaly.

https://doi.org/10.5194/tc-2019-129
Preprint. Discussion started: 25 June 2019

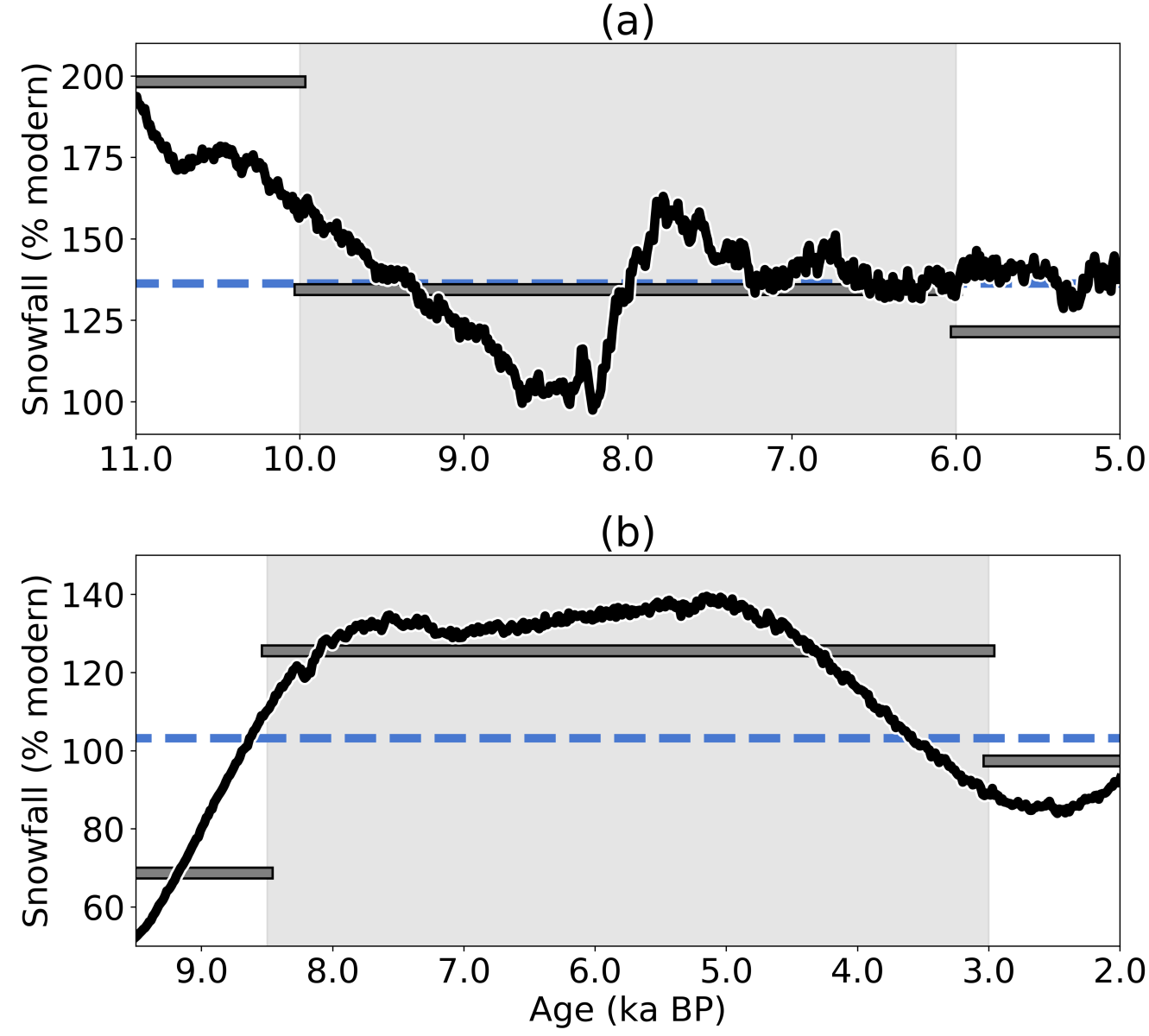

Figure 7. Average snowfall across the northern and southern flowlines during the HTM, expressed as a percentage of modern, for the Buizert et al. (2018) (a) and (Dahl-Jensen et al., 1998) (b) temperature inversions. The HTM for each reconstruction is shaded gray. Gray lines show average snowfall prior, during, and after the HTM. Average Holocene snowfall is indicated by blue dashed lines.

https://doi.org/10.5194/tc-2019-129
Preprint. Discussion started: 25 June 2019

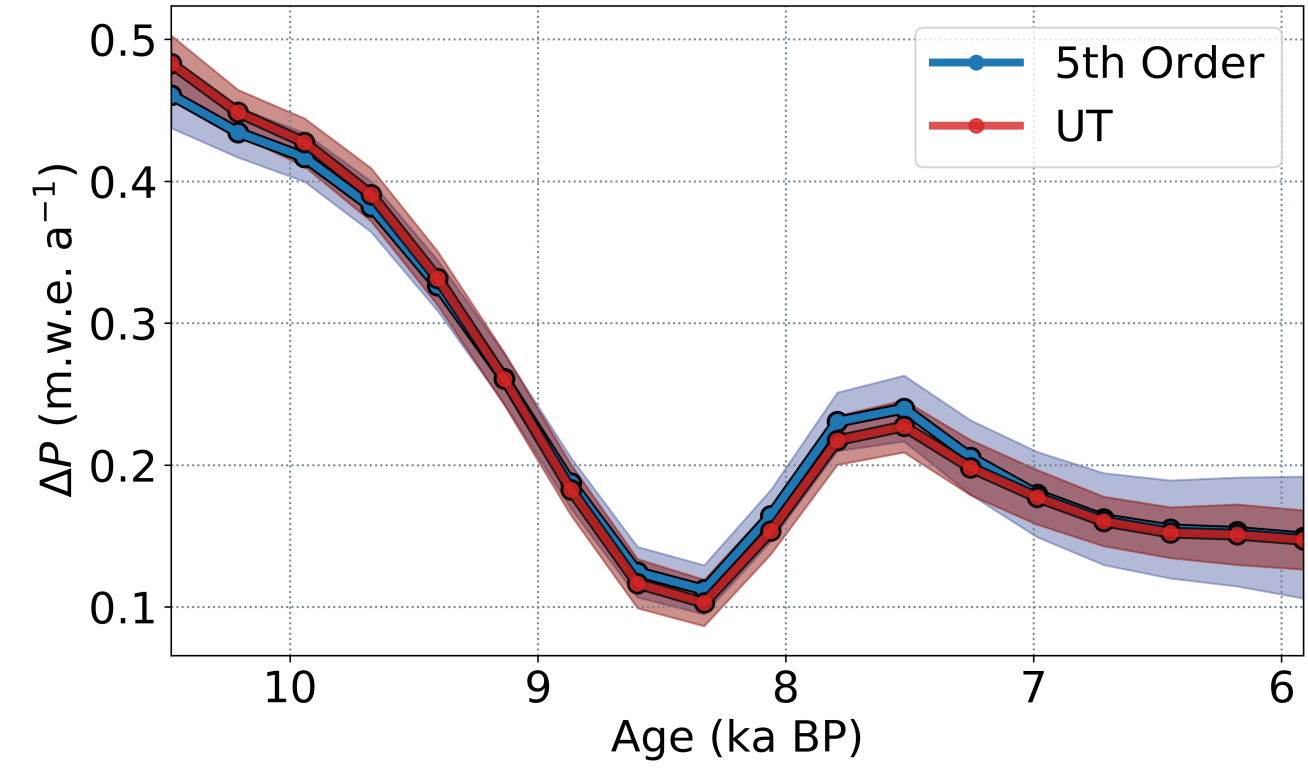

Figure 8. Estimates of the precipitation anomaly ΔP on the southern flowline during the Buizert et al. (2018) HTM. Red and blue lines / 95% confidence bands show ΔP estimates for the UT and a fifth order cubature method respectively.

https://doi.org/10.5194/tc-2019-129
Preprint. Discussion started: 25 June 2019

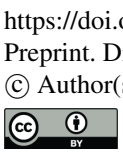

The Cryosphere
Discussions
Open Access
EGU

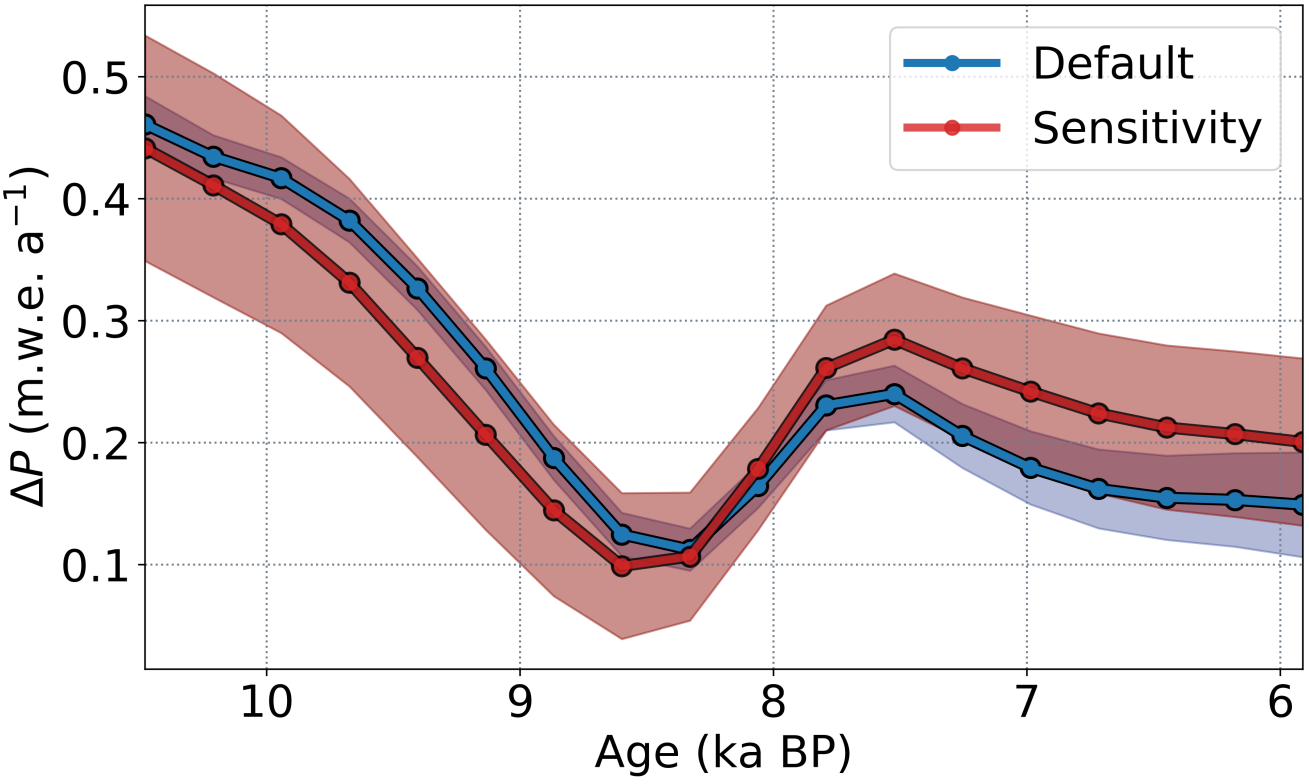

Figure 9. Estimates of the precipitation anomaly ΔP on the southern flowline during the Buizert et al. (2018) HTM. Red and blue lines / 95% confidence bands show ΔP estimates for the sensitivity experiment (accounting for uncertainties in the ice flow and PDD model parameters) and a default inversion (which uses a fixed parameter set) respectively.